# An In Situ ATR-FTIR Electrochemical Cell for the Study of Battery Processes: Design, Implementation, and Data Analysis

Daniela Josepetti, Ilie Hanzu, Nicolas Louvain, Lorenzo Stievano, Long Hoang Bao Nguyen

*Chemistry - Methods*

Chemistry—Methods

Chemistry Europe
European Chemical Societies Publishing

RESEARCH ARTICLE OPEN ACCESS

# An In Situ ATR-FTIR Electrochemical Cell for the Study of Battery Processes: Design, Implementation, and Data Analysis

Daniela M. Josepetti[1,2] | Ilie Hanzu[3] | Nicolas Louvain[1,2] | Lorenzo Stievano[1,2] | Long Hoang Bao Nguyen[1,2]

[1]Institut Charles Gerhardt Montpellier (ICGM), Univ. Montpellier, CNRS, ENSCM, Montpellier, France | [2]Réseau sur le stockage électrochimique de l'Énergie (RS2E), CNRS, Amiens, France | [3]Institute for Chemistry and Technology of Materials, Graz University of Technology, Graz, Austria

**Correspondence:** Lorenzo Stievano (lorenzo.stievano@umontpellier.fr) | Long Hoang Bao Nguyen (long-hoang-bao.nguyen@umontpellier.fr)

**Received:** 10 October 2025 | **Revised:** 8 December 2025 | **Accepted:** 8 December 2025

**Keywords:** attenuated-total-reflectance Fourier-transform infrared | interfacial chemistry | lithium-ion batteries | operando spectroscopy | solid–electrolyte interphase

## ABSTRACT

Phenomena occurring in the electrolyte as well as the interfaces with the electrodes, such as $Li^+$ solvation/desolvation and solid–electrolyte interphase formation, govern the performance and safety of Li-ion batteries. In this article, a dedicated, spring-loaded *operando* attenuated-total-reflectance Fourier-transform infrared cell is presented, enabling quantitative, time-resolved probing of the electrode–electrolyte processes under electrochemical examination. The optical design is based on a 45° incidence diamond waveguide, while the electrochemical setup comprises a gas-tight stainless steel body. The procedure for preparing the self-supported electrode and the acquisition protocol are also presented, together with a reproducible analysis workflow for tracking solvated versus free electrolyte solvent species without baseline subtraction. Representative measurements on composite tin electrodes validate the ability of the setup to resolve band shifts and intensity changes linked to $Li^+$ coordination and electrolyte reduction. The methodology generalizes to diverse negative-electrode chemistries and provides molecular-level insight into battery phenomena under electrochemical operating conditions.

## 1 | Introduction

Independent of the specific electrode chemistry, lithium-ion batteries (LIBs) commonly operate through coupled bulk and interfacial processes [1]. At negative electrodes, the electrolyte is partially reduced at low potential to form the solid–electrolyte interphase (SEI) [2], while $Li^+$ are continuously solvated/desolvated at the interface during (de)lithiation of the electrode materials [3]. The structure and composition of the electrode, and the dynamics of these interfacial processes govern Coulombic efficiency, impedance growth, safety, and eventually the lifetime of LIBs [4, 5]. Capturing these interfacial phenomena in their native electrochemical environment is essential to understand the battery operation and degradation mechanism. Therefore, *operando* approaches are required to obtain time-resolved and chemically specific information under realistic battery cycling conditions [6], moving beyond *postmortem* analyses that may modify these interfacial processes. These modifications may originate from intermediate evaporation of the electrolyte solvent [7], precipitation of solvated species [8], or simply from relaxation of ongoing reactions since the electrode has been extracted from the battery [9]. Commonly, washing steps are used to remove excess electrolyte signal; however, they may also remove SEI components [10].

Fourier Transform Infrared spectroscopy (FTIR) in attenuated total reflection (ATR) geometry provides a direct sensitivity to interfacial molecular vibrations within the evanescent field and is naturally compatible with sealed electrochemical cells. In situ/*operando* FTIR–ATR has been used to reveal electrolyte dynamic effects [11], distinct reduction mechanisms on the

electrode surface [10], and thermal degradation of the electrolyte [12]. Through thin-film model systems, the presence of polymerization products and the evolution of SEI thickness during cycling were also observed [13]. *Operando* ATR-FTIR has been shown to be capable of tracking the evolution of free and solvated carbonate solvent molecules during electrode reactions, offering a sensitive probe on the interfacial solvation process and electrolyte reduction mechanism [14]. Furthermore, nanoscale infrared analysis has revealed the chemical heterogeneity of SEI layers on alloying electrodes such as tin, motivating the development of characterization approaches that average over relevant areas while preserving chemical specificity [15].

Guided by these advances, the present work focuses on the development of an *operando* ATR-FTIR methodology for studying battery processes, which is based on a robust, spring-loaded stainless steel cell architecture that maintains optical contact during morphological changes. This setup also allows environmental control (purge and temperature stabilization) to minimize baseline drift, and is complemented by a time-resolved acquisition protocol. A conservative data analysis method that preserves proportionality between band intensities and interfacial concentration changes is also proposed. By combining (i) a modular cell with interchangeable ATR crystals, (ii) an integrated temperature control, and (iii) an openly described data-processing strategy adapted to high-density *operando* datasets, this work bridges the gap between proof-of-concept ATR cells and broadly usable *operando* workflows.

This comprehensive technical and methodological setup aims to facilitate the adoption of *operando* ATR-FTIR as a routine diagnostic tool for interfacial chemistry in LIB electrode development. For this purpose, we offer a transparent, reproducible protocol that complements more demanding structural probes and nanoscale imaging.

## 2 | Methods

### 2.1 | Spectroscopic Configuration and Environmental Control

Mid-IR spectra (4000–500 $cm^{-1}$) were acquired on a Thermo Scientific Nicolet iS50-FT-IR® spectrometer equipped with a KBr beam splitter, a liquid nitrogen cooled mercury cadmium telluride detector with a resolution of 4 $cm^{-1}$, and an ATR probe from Harrick® (MVP-PRO), on which the in situ cell is directly built. To increase the signal-to-noise ratio, 32 interferograms are coadded per spectrum, resulting in a 30 s acquisition to avoid loss of time resolution. The spectrometer and cell enclosure are continuously purged to suppress atmospheric $H_2O/CO_2$ bands, and the cell temperature is regulated with an external water bath to reduce baseline drift and stabilize band positions (Figure 1).

### 2.2 | In Situ Cell Setup

The cell consists of two sealing components (Figure 2a): an O-ring ensuring contact between the stainless steel plate supporting the ATR diamond and the stainless steel cell body, and a Swagelok®-type ferrule between the cell body and the plunger. A single-reflection diamond ATR element (5 x 3 mm) is used for the collection of the IR signal. The electrochemical cell is an in situ type in which it is possible to perform *operando* IR spectra acquisition [16]. The cell assembly sequence for *operando* IR spectroscopy measurements is similar to that widely used in a coin cell configuration, as illustrated in Figure 2b. Special attention is given to the component in contact with the ATR probe, as only the material in close contact with it is analyzed. The cell assembly was carried out inside an Ar-filled glovebox to avoid contact between electrolytes and ambient air.

The IR beam impinges at 45°, yielding an evanescent-field penetration depth of order the mid-IR wavelength, as calculated with (Equation (1)).

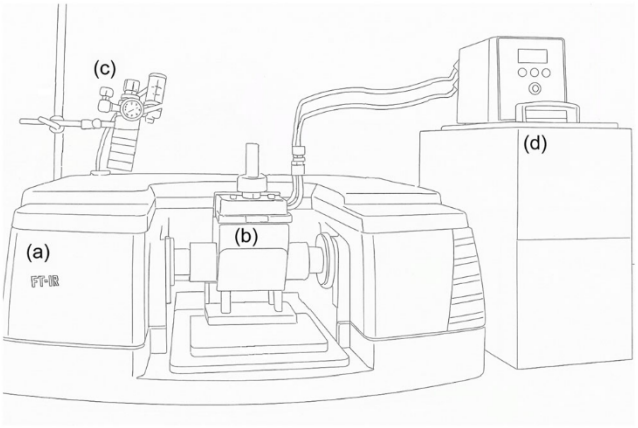


**FIGURE 1** | Attenuated Total Reflection Infrared Setup for *operando* measurement: (a) FTIR spectrometer; (b) ATR probe with custom-developed cell; (c) manometer and air flow controller; (d) water bath for temperature regulation.

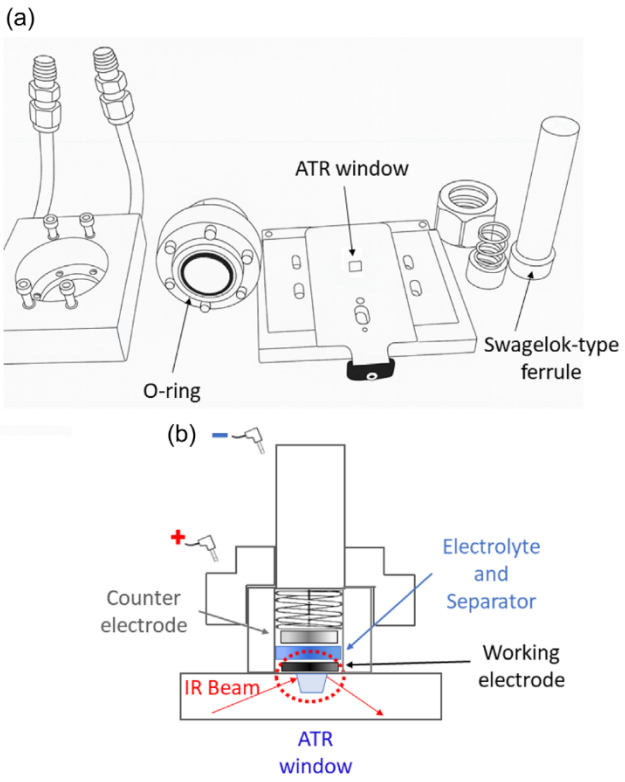


**FIGURE 2** | In situ ATR-FTIR cell hardware: (a) exploded view and (b) assembled body. Spring-loaded plunger ensures optical contact; O-rings provide gas-tight sealing.

**TABLE 1** | Probing depth (μm) estimation for different conditions.

| Wavenumber, $cm^{-1}$ | EC:DEC 1 M $LiPF_6$ | EC:DEC 1 M $LiPF_6$ 5% FEC | EC:DEC 1 M $LiPF_6$ 2% VC | DME:DOL 1 M LiTFSI |
|---|---|---|---|---|
| 3000 | 0.547 | 0.546 | 0.547 | 0.542 |
| 2000 | 0.820 | 0.819 | 0.820 | 0.813 |
| 1500 | 1.094 | 1.092 | 1.093 | 1.084 |
| 1000 | 1.640 | 1.638 | 1.640 | 1.626 |
| 500 | 3.281 | 3.276 | 3.280 | 3.252 |

$$d_e = \frac{\lambda}{2\pi\sqrt{n_d^2 \sin^2\theta - n_s^2}} \quad (1)$$

Here, $\lambda$ is the wavelength, $\theta$ is the incidence angle, and $n_d$ and $n_s$ are the refractive indices of the ATR crystal and the sample, respectively.

The refractive index is considered constant for the wavelength, given that the applied IR range (2500–20,000 nm) results in an almost constant refractive index according to Cauchy's equation (Equation (2)) [17].

$$n(\lambda) \approx A + \frac{B}{\lambda^2} + \frac{C}{\lambda^4} + \ldots \quad (2)$$

Furthermore, the considered refractive index for carbonate-based electrolytes was obtained from the literature [18–23].

The probing depth of IR beam in some common electrolytes for LIBs is calculated and presented in Table 1. Figure 3 reveals the evolution of the penetration depth ($d_e$) across the entire IR range for LP30 electrolyte. According to the estimation results, the penetration depth for this IR configuration ranges from ≈0.5 to 3.3 μm and does not vary significantly between different electrolyte formulations. In this context, considering that the surface region is typically within 0.1–10 nm [2], the in situ cell setup allows for bulk analysis of the electrolyte/electrode, while surface-specific phenomena (such as adsorption, formation of the first layers of the SEI, lithium plating/stripping, and so on) are not directly probed. Despite these limitations, this IR configuration enables direct analysis of the battery processes through the electrolyte. It allows monitoring local variations in electrolyte concentration, providing insight into electrolyte transport and dynamics during the electrochemical process. In addition, it enables the detection of new dissolved species formed at the electrode interface (Table 2).

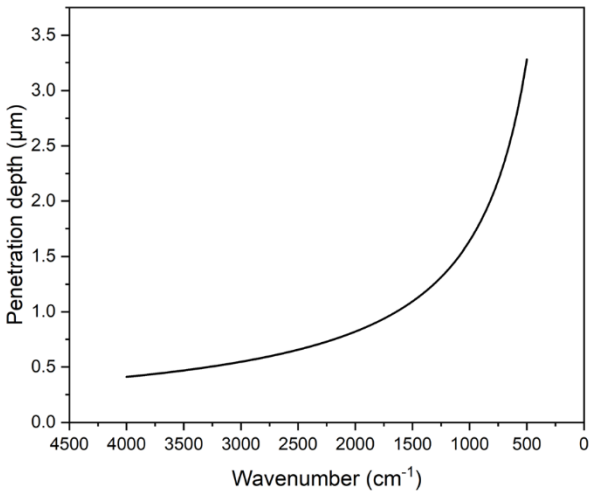


**FIGURE 3** | Penetration depth ($d_e$) in the IR energy range 4000–500 $cm^{-1}$ calculated for the LP30 electrolyte.

## 2.3 | Electrode Preparation for Electrolyte Degradation Studies

Tin, one of the two most studied alloy negative electrode materials for LIBs, was selected for this study. The lithiation of tin results in the formation of $Li_{22}Sn_5$, corresponding to a theoretical capacity of 994 mAh/g; nonetheless, the integration of tin in LIBs is highly challenging because of its catalytic activity towards electrolyte degradation, inducing cell failure with prolonged cycling [10]. Nano-tin was used in the *operando* experiment because of its high surface area, which can enhance electrolyte degradation up to a limit that can be observed easily by *operando* ATR-FTIR. Self-supported electrodes were prepared via a conventional electrode fabrication procedure [24]. A slurry consisting of 75 wt% nano-tin active material, 15 wt% polyvinylidene fluoride (PVDF) binder, and 10 wt% C65 acetylene black conductive additive in N-methyl-2-pyrrolidone (NMP) was cast on a Cu foil using a doctor blade with a wet gap of 1.75 mm. After drying in air, the resulting cohesive and homogeneous film was detached from the Cu foil, calendared in a roll press using a 10 mm gap, punched into Ø 8 mm discs, and further vacuum dried for 12 h at 70°C. For such electrodes, an active material mass loading of 8.14 ± 0.6 mg was obtained.

X-ray diffraction (XRD) characterization of the nano-tin electrodes was carried out on a PANalytical X'Pert Pro-MPD diffractometer equipped with the Cu Kα1,2 radiation, revealing the presence of two crystalline phases: β-Sn and SnO (Figure 4a).

Scanning electron microscopy-energy dispersive X-ray (SEM-EDX) analysis of morphology and composition was carried out on a Hitachi S-4800 electron microscope. SEM analysis revealed

**TABLE 2** | Room temperature $^{119}Sn$ Mössbauer hyperfine parameters for the Sn nanoparticles.

| Site | $\Delta$, mm/s | $\delta$, mm/s | $\Gamma$, mm/s | Area, % |
|---|---|---|---|---|
| $Sn^{+4}$ | 0.51 | 0.14 | 0.97 | 29 |
| Sn metal | 0.20 | 2.55 | 1.17 | 56 |
| $Sn^{+2}$ | 1.38 | 2.70 | 0.90 | 15 |

Note: $\Delta$, quadrupole splitting; $\delta$, isomer shift; $\Gamma$, full linewidth at half maximum; Area, relative resonance area.

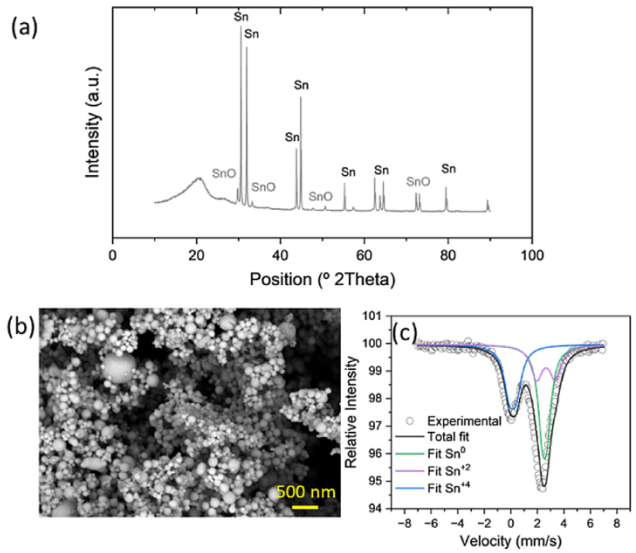


**FIGURE 4** | Characterization of nano-tin powder. (a) XRD pattern and phase identification. (b) SEM image. (c) Room temperature $^{119}$Sn Mössbauer spectrum.

a particle size distribution spanning from 40 to 400 nm, with an average value of ≈80 nm (Figure 4b), while an average atomic composition of 61% Sn, 26% O, and 13% C was obtained by EDX. It must be noted that the carbon tape used in the SEM-EDX analysis may substantially contribute to the carbon and oxygen signals.

Transmission $^{119}$Sn Mössbauer spectra were collected at room temperature with a constant acceleration spectrometer using a $Ca^{119m}SnO_3$ source. A LiF scintillation detector was employed for the detection of the $\gamma$-rays. The velocity scale was calibrated with a high-purity $\alpha$-Fe foil at room temperature using a $^{57}$Co:Rh source. Isomer shifts are given relative to the $CaSnO_3$ source. Three spectral components attributed to Sn metal (56%), $Sn^{4+}$ (29%), and $Sn^{2+}$ (15%) (2) were identified in the room temperature $^{119}$Sn Mössbauer spectrum of the nano-tin powder (Table 2). Considering the much lower Lamb–Mössbauer factor of tin metal compared to oxidized tin species (about five and ten times lower than that of SnO and $SnO_2$ at 300 K, respectively) [25], these results indicate that a large majority of the nano-tin powder contained in the electrodes (≈90%) is composed of tin metal, the remainder being represented by a minority of oxidized $SnO_x$ species (mostly SnO).

## 2.4 | Electrochemical Cell Assembly

Half-cells were prepared with the self-supported nano-tin electrode versus Li metal. The two electrodes were separated by a Whatman glass-fiber disk soaked with an electrolyte containing 1 M $LiPF_6$ dissolved in a 1:2 volume mixture of ethylene carbonate (EC) and diethyl carbonate (DEC). Whatman glass-fiber was preferred as a separator as its higher electrolyte volume intake enables improving the electrochemical performance under these experimental conditions, and also because it does not produce additional bands in the evaluated IR spectra range.

## 2.5 | Data Acquisition and Processing

A crystal/air reference spectrum ($R_0$) is acquired at the beginning of each measurement. Spectral absorbance is expressed as $Abs = \log_{10}(R_0/R)$, where $R$ is the crystal/electrode reflectance. This definition avoids arbitrary baseline operations and preserves the proportionality between integrated intensities and interfacial concentration changes within the evanescent field.

Unless stated otherwise, 32 interferograms were coadded per spectrum at 4 $cm^{-1}$ resolution. For baseline stability tests, one spectrum every 15 min was recorded under open circuit voltage (OCV), that is, before starting electrochemical cycling. For *operando* sequences, a 15-min cadence was applied during the chronoamperometry experiment. These experimental conditions allow spectrum collection with a reasonable signal-to-noise ratio while ensuring the monitoring of temperature control, maintained at 25°C, and contact stability of the in situ cell. Continuous purging of the spectrometer and cell enclosure limits atmospheric $H_2O$ and $CO_2$ fluctuations, thereby improving signal stability when using either the laboratory dry-air circuit or an artificial-air cylinder feed (Figure 5). As a result, it was observed that the variation in $CO_2$ signals is more important under facility air, whereas water bending mode signal persists under cylinder air, and the diamond background evolves independently in both cases. The *operando* setup was therefore standardized on laboratory dry air with sufficient purge time before any acquisitions. Baseline evolution was nevertheless explicitly monitored with extended OCV tests as well as during slow cycling.

Band assignment (cf. Table 3) was conducted on the preliminary measurement of reference spectra of EC, DEC, and $LiPF_6$ solutions in these solvents and based on literature [12, 26–31]. The splitting of the stretching vibrational band of EC's carbonyl group is the result of Fermi resonance [28]. Free versus $Li^+$-solvating carbonate species are discriminated by diagnostic shifts in $\nu_{C=O}/\nu_{C-O}$. By tracking peak positions (local maxima or local fits) and integrated areas or peak heights, modifications in chemistry and composition of the species contained in the probed electrolyte volume near the electrode surface can be tracked. The band ratio between free and solvating species allows a semi-quantitative

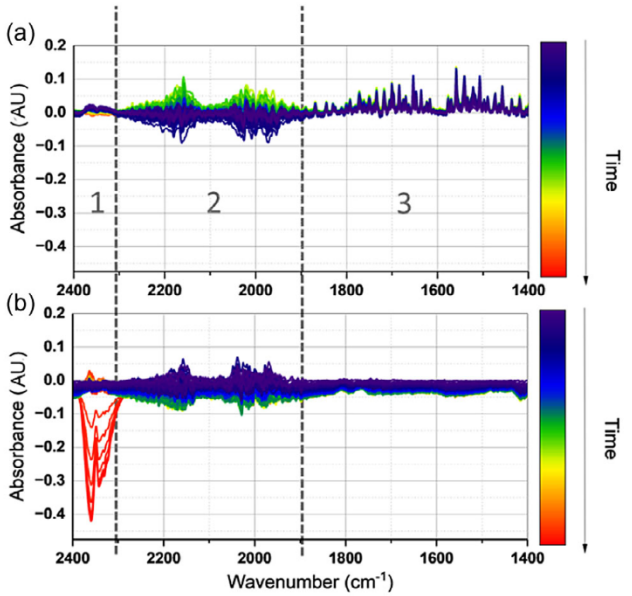


**FIGURE 5** | *Operando* measurement to monitor air purge contributions in the infrared spectra. (a) Cylinder. (b) Laboratory facilities (1 spectrum every 15 min).

**TABLE 3** | Assignment of characteristic vibrational bands observed in the IR spectrum of the EC:2DEC 1 M $LiPF_6$ solvent in the 2000–700 $cm^{-1}$ range.

| Vibrational mode, $cm^{-1}$ | Band |
|---|---|
| 1804 and 1771 | $\nu$(C═O) of EC |
| 1740 | $\nu$(C═O) of DEC |
| 1714 | $\nu$(C═O) of DEC coordinated to $Li^+$ |
| 1482 | $\delta_{scissor}(CH_2)$ of EC |
| 1469 | $\delta_{sciss}(CH_2)$ of DEC |
| 1448 | $\delta_{as}(CH_3)$ of DEC |
| 1407 | $\delta_{wag}(CH_2)$ of EC coordinated to $Li^+$ |
| 1390 | $\delta_{wag}(CH_2)$ of EC |
| 1375 | $\delta(CH_3)$ of DEC |
| 1302 | $\nu_{as}$(OCO) of DEC coordinated to $Li^+$ |
| 1259 | $\nu_{as}$(OCO) of DEC |
| 1196 | $\nu_{as}$(OCO) and $\delta_{wag}(CH_2)$ of EC coordinated to $Li^+$ |
| 1159 | $\nu_{as}$(OCO) and $\delta_{wag}(CH_2)$ of EC |
| 1070 | $\nu_s$(OCO) of EC |
| 1017 | $\nu_s$(CCO) of DEC |
| 840 | $\nu_s$(P—F) of $PF_6^-$ |
| 792 | $\gamma$(C—H) out-of-plane deformation of DEC |
| 773 | $\gamma$(C═O) out-of-plane of ring of EC |
| 728 | $\delta$(ring) of EC coordinated to $Li^+$ |
| 716 | $\delta$(ring) of EC |

estimation of the local $Li^+$ concentration gradients at the ATR probe.

## 2.6 | Data Analysis

### 2.6.1 | Direct Observation and Difference Spectra

Different approaches were used for the analysis of the collected *operando* IR data. The first one relies on a direct utilization of absorbance versus wavenumber plots, as seen in Figure 6a. During the operation of an in situ cell, certain electrolyte/solvent species may be consumed, while new species may be formed, for example, electrolyte degradation products. The change in the amount of each chemical species will lead to a variation in the intensity of their corresponding vibrational modes, according to the Beer–Lambert's law ($A = \varepsilon\, c\, l$, where $A$ is the absorbance, $\varepsilon$ is the molar absorptivity, $c$ is the concentration/amount of the species of interest, and $l$ is the path length).

In certain cases, when the modifications in the IR signals during cycling are subtle and difficult to spot, a difference approach can be employed. In this approach, a reference spectrum is selected among those recorded (e.g., the last OCV spectrum) and the difference is calculated using the relation $(A(t) - A(0))$. This method enhances even minor modifications, making them easier to observe. Depending on the choice of the reference $A(0)$, the

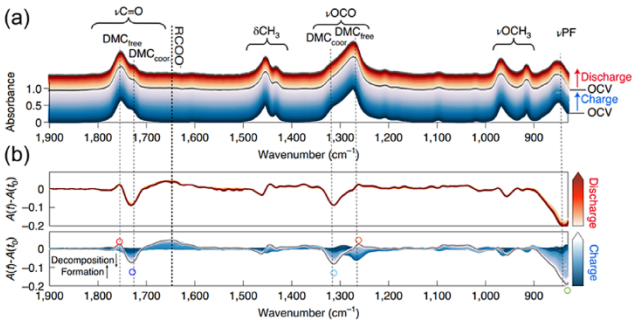


**FIGURE 6** | Examples of *operando* infrared data processing reported in the literature, where $A(t)$ is the absorbance spectrum at a given time (a), which is subtracted from a reference absorbance spectrum at $t = 0$ ($A(t_0)$), resulting in the relative evolution of absorbance $(A(t) - A(t_0))$ (b). Reproduced with permission from Ref. [32].

appearance or disappearance of a particular chemical species will result in a positive or negative signal, respectively. An example can be seen in Figure 6b, where the identification of new products and the decomposition of other species are more easily resolved in this way.

### 2.6.2 | Temporal Evolution of *Operando* Spectra

To further compare the temporal evolution of different chemical species/vibrational modes, two-dimensional correlation spectroscopy (2D-IR) plots can be used [33]. The 2D-IR map displays a wavenumber versus wavenumber matrix constructed from a time-resolved infrared dataset, emphasizing vibrational bands that develop either concurrently (synchronous plot) or independently (asynchronous plot) over time.

The synchronous plot exhibits bands that increase or decrease simultaneously. A positive cross-peak indicates that the intensities of both bands are increasing or decreasing together. In contrast, a negative cross-peak suggests that as one band increases in intensity, the other decreases [34].

The asynchronous plot, on the contrary, shows if two bands are involved in nonsimultaneous processes. For a positive asynchronous cross-peak, the spectral change in band one ($x$-axis) precedes that of band two ($y$-axis) when the corresponding synchronous correlation between these bands is also positive. If the asynchronous cross-peak is negative, then the modification in band one follows that of band two. This logic is inverted when the corresponding synchronous cross-peak is negative. These plots help to separate overlapping bands and identify distinct time-dependent processes [34].

To illustrate the application of 2D-IR data, Figure 7 shows the evolution of vibrational bands of propylene carbonate (PC) as the concentration of LiTFSI increases (mole fraction 0–0.4). In Figure 7a, the band at 1788 $cm^{-1}$, associated with $\nu$(C═O) in free PC, decreases in intensity with increasing salt concentration (reflecting the reduction of free PC), while the band at 1773 $cm^{-1}$, corresponding to the $\nu$(C═O) stretching modes involved in $Li^+$ solvation, increases. In Figure 7b, the asynchronous plot highlights cross-peaks 2, 3, 4, and 6 (1804, 1790, 1766, and 1733 $cm^{-1}$), which deviate from ideal solution behavior and reveal the dynamics of LiTFSI clustering in solution. The asynchronous data further indicate that these solvation-related peaks (2, 3, 4, and 6) appear after the changes of the PC vibrational modes.

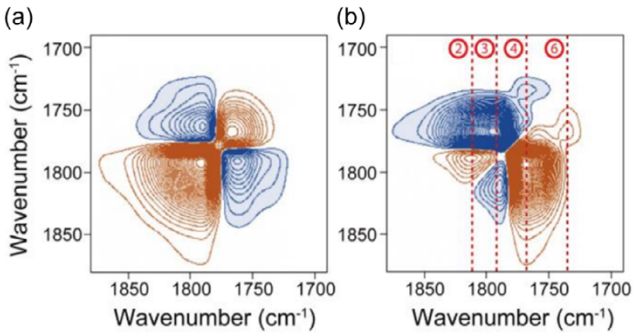


**FIGURE 7** | Example of two-dimensional correlation spectroscopy for infrared data processing, reproduced with permission from Ref. [35]. The (a) synchronous and (b) asynchronous 2D-IR spectra of $\nu$(C═O) region in the process of increasing concentration of LiTFSI. Red and blue backgrounds represent positive and negative correlation intensities, respectively.

## 3 | Results

A representative test for validating the *operando* ATR setup was carried out in potentiostatic mode. First of all, a systematic baseline tracking was carried out under OCV, showing an absolute absorbance drift smaller than ~0.05 absorbance units over several hours. Once a stable OCV spectrum was reached, the potential was rapidly decreased and held at 0.75 V. The spectra collected with a cadence of 2.5 h, shown in Figure 8, reveal a local decrease over time of the bands related to solvated species in the electrolyte (i.e., DEC and EC solvating $Li^+$), centered at 1714 and 1196 $cm^{-1}$, as well as to the salt anion at 840 $cm^{-1}$. On the contrary, bands related to free EC and DEC, appearing at 1740 and 1259 $cm^{-1}$, show a local increase over time.

The decrease in intensity of the Li-solvating EC and DEC bands, as well as those of the salt anion, can be attributed to the reduction in potential, which triggers several modifications at the surface of the ATR probe in the vicinity of the nano-tin electrode surface. At this voltage, the expected ongoing reactions are the reduction of $SnO_x$ species and possible reactions related to electrolyte degradation, since the formation of Li–Sn alloys starts only below 0.6 V [36]. A local decrease in the concentration of $Li^+$ is observed, consumed by the ongoing reactions at the surface of the electrode. As $Li^+$ is consumed, the local concentration of free solvent molecules increases, as they are released from $Li^+$ solvation. The counter-anion concentration decreases to preserve electroneutrality locally in the probed solution.

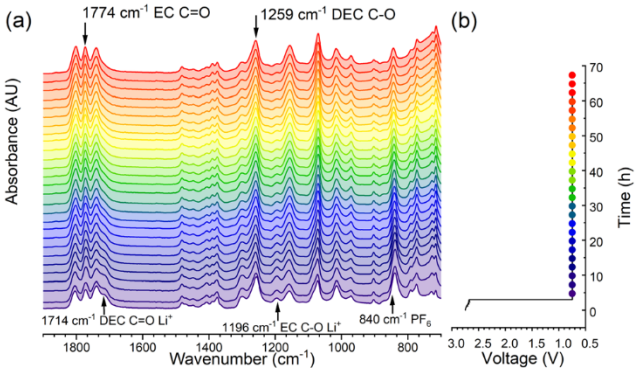


**FIGURE 8** | *Operando* infrared monitoring of nano-tin electrode at constant potential (1 Spectrum/2.5 h). (a) IR spectra evolution. (b) Electrochemical data.

Additionally, the plot exhibits a baseline drift below 800 $cm^{-1}$. It may represent changes in the refractive index of the sample in contact with the ATR probe, resulting from electrochemically induced processes. Applying a potential alters the ionic distribution, changes the solvent orientation in the electric double layer, and forms products for reactions activated by such a potential. These variations are expected to be more pronounced at lower wavenumbers, as the penetration depth is greater in this region. Nevertheless, it cannot be excluded that changes in the electronic conductivity of the electrode, the appearance of additional bands related to new degradation products, instrumental variability, temperature, or pressure may have caused the observed drift.

Further modifications which are not readily visible in this type of data representation, may be spotted using alternative $A(t) - A(0)$ difference spectra, as the example shown in Figure 9 where the last spectrum measured at OCV is selected as $A(0)$. In this new representation, the behavior of bands related to solvent coordinated with $Li^+$ and free solvent in response to an electrochemical stimulus is more easily observed: here, positive bands represent an increase in local concentration, whereas a decrease in concentration is portrayed as negative bands. Additional advantages are indicated as: the prompt deconvolution of certain bands, for instance the band at 1765 $cm^{-1}$ with negative intensity assigned for the $\nu$(C═O) stretching mode of EC coordinated with $Li^+$, corresponding to the broadening of band 1771 $cm^{-1}$ caused by $Li^+$ coordination (cf. Figure S3), as confirmed by earlier works [26]; and the identification of possible new products, as the growth of band 910 $cm^{-1}$ and the broadening of the band at 893 $cm^{-1}$, which is related to the EC breathing mode. The signal growth in the region below 800 $cm^{-1}$ is not necessarily associated with product growth and is likely due to baseline drift (*vide supra*). Therefore, these features should be taken into account when using the $A(t) - A(0)$ representation to avoid misleading conclusions.

The synchronous 2D-IR plot (Figure 10a), similar to $A(t) - A(0)$, highlights the opposite behavior of electrolyte solvent molecules when coordinated or uncoordinated with $Li^+$ ions, as they produce distinct signals compared to other bands in this representation. For example, the band at 1714 $cm^{-1}$ (point d in Figure 10a, assigned to the $\nu$(C═O) stretching of DEC coordinated with $Li^+$) shows a positive correlation with the band at 840 $cm^{-1}$, indicating that both vary in the same direction, that is, they simultaneously decrease in intensity. In contrast, the band at 1740 $cm^{-1}$ (point c in Figure 10a, attributed to pure DEC $\nu$(C═O) stretching) exhibits a negative correlation with the 840 $cm^{-1}$ band, indicating that when the first increases in

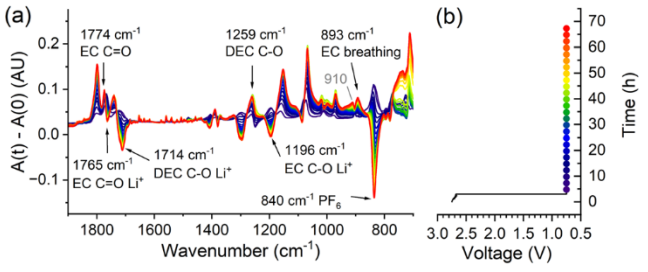


**FIGURE 9** | *Operando* infrared monitoring of nano-tin electrode at constant potential (1 Spectrum/2.5 h) for difference absorbance plot, where $A(t)$ is the absorbance spectrum at a given time, which is subtracted from a reference absorbance spectrum at $t = 0$ (the last IR spectrum in OCV), resulting in the relative evolution of absorbance ($A(t) - A(0)$). (a) IR spectra evolution. (b) Electrochemical data.

intensity, the other decreases. Moreover, it clearly demonstrates that most of the electrolyte band evolution under *operando* conditions arises from a single process, directly related to the constant potential applied to the system.

The asynchronous 2D-IR spectrum (Figure 10b) reveals the sequence of spectral changes. For instance, both the 1714 and 1740 $cm^{-1}$ bands exhibit a positive asynchronous correlation with the 1159 $cm^{-1}$ band (point f in Figure 10b, assigned to the uncoordinated EC $\nu$(C—O) stretching). In this sense, lithium desolvation processes occur before, as expected, due to the interfacial nature of electrolyte reduction. For the relation with the 1714 $cm^{-1}$ band, since the synchronous correlation is negative, the modification of the $Li^+$-coordinated DEC $\nu$(C═O) stretching occurs before that of the free $\nu$(C—O) stretching. Similarly, for the 1740 $cm^{-1}$ band, as the synchronous correlation is positive, the changes of free DEC C═O stretching mode are after those in the free EC C—O stretching mode. EC may respond more quickly to potential stimuli, either by solvation or electrolyte degradation phenomena. This corresponds to the classical behavior of EC versus linear carbonates, where the former would decompose before other carbonate species [37].

## 4 | Discussion

The results of the cell test presented above imply several consequences.

First of all, the stable intensity of the spectra even after a long period of time emphasizes the robustness of the in situ cell in terms of signal reproducibility, and demonstrates that such a setup maintains optical contact even over multihour experiments. The spring-loaded cell design and the standardized sealing (body-plunger and ATR-electrode O-rings) are essential to suppress spurious baseline evolution, while purge/temperature control reduced atmospheric contributions to a manageable, slowly varying background. Along with the optimization of the cell setup, it was found that several other minor parameters should be taken into account to allow for reproducible, stable results with a barely shifting baseline.

1. Controlling electrode positioning with respect to the ATR probe is extremely important to recover the electrolyte signal in the vicinity of the electrode, but also in its bulk if desired.
2. Direct contact of an electron-conducting electrode with the ATR probe leads to a strong decrease in the intensity and broadening of vibration bands. This happens both with metallic electrodes and with other materials mixed with carbon additives. These materials, in fact, inherently display strong broadband absorption, arising from their electronic conductivity and lattice vibrations, which lead to baseline shifts and partly obscure the vibrational features of the material under investigation. This effect can be mitigated by using thin films or self-supported composites.

Moreover, the increase/decrease and shifts of carbonate $\nu$(C═O)/$\nu$(C—O) bands can be used to build simple markers:

1. Solvated/free intensity ratios can be used to represent interfacial $Li^+$ coordination.
2. Integrated absorbance of selected bands can be used as an index of interfacial $Li^+$ concentration in the electrolyte.

These markers are robust and can also be used in cases of small baseline fluctuations, enabling comparisons between independent experiments.

Additionally, one inherent limitation is related to the depth of the probe used in the ATR method. In fact, the probing depth of the order of a few µm averages over multiple layers, and the detection of nm-resolved SEI composition is virtually impossible.

Finally, this approach, presented here in the case of Sn nanoparticle electrodes, can be generalized to other negative electrodes such as intermetallics, alloys, or hard carbons, if adequate IR transparency and mechanical integrity during cycling are ensured.

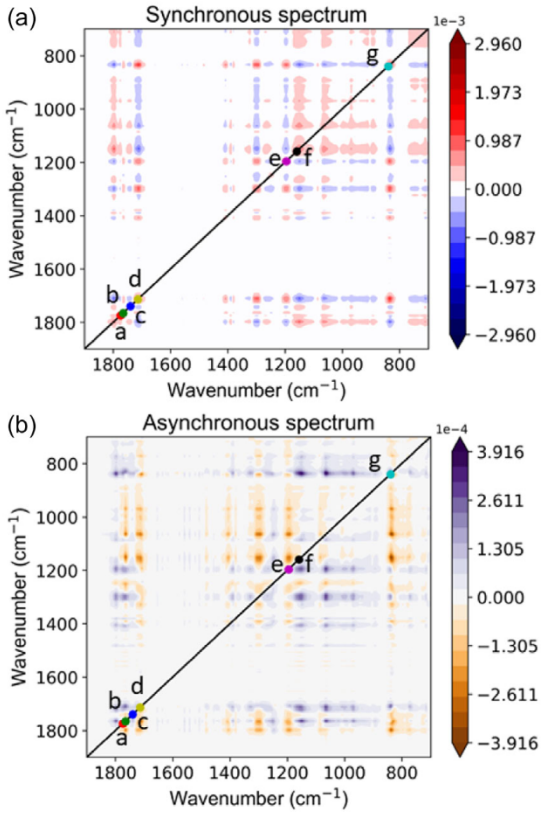


**FIGURE 10** | Two-dimensional correlation spectroscopy for infrared data of nano-tin electrode at constant potential. (a) Synchronous correlation. (b) Asynchronous correlation.

## 5 | Conclusion

A transferable *operando* ATR-FTIR methodology, comprising cell design, a dedicated acquisition protocol, and an analysis workflow is presented, enabling the time-resolved study of electrode–electrolyte interfacial chemistry during battery operation. The sensitivity of this method to solvation/desolvation dynamics near the electrode surface, the evaluation of kinetic ordering of molecular events, and the detection of reduction products make it a valuable complement to structural *operando* probes.


### Acknowledgments

As part of the DESTINY PhD Programme, D.M.J. acknowledges funding from the European Union's Horizon 2020 Research and Innovation Programme under the Marie Skłodowska-Curie Actions COFUND

(Grant Agreement #945357). Funding from the French National Research Agency (STORE-EX Labex Project ANR-10-LABX-76-01) is gratefully acknowledged.

## Funding

This work was supported by the Horizon 2020 Research and Innovation Programme (Grant 945357) and Agence Nationale de la Recherche (Labex STOREX, Grant ANR-10-LABX-76-01).

## Conflicts of Interest

The authors declare no conflicts of interest.

## Data Availability Statement

The data that support the findings of this study are available from the corresponding author upon reasonable request.

## References

1. Y. Ji, Z.-W. Yin, Z. Yang, et al., "From Bulk to Interface: Electrochemical Phenomena and Mechanism Studies in Batteries via Electrochemical Quartz Crystal Microbalance," *Chemical Society Reviews* 50, no. 19 (2021): 10743–10763.

2. E. Peled and S. Menkin, "SEI: Past, Present and Future," *Journal of the Electrochemical Society* 164, no. 7 (2017): A1703.

3. M. Winter, "The Solid Electrolyte Interphase–the Most Important and the Least Understood Solid Electrolyte in Rechargeable Li Batteries," *Zeitschrift fuer Physikalische Chemie* 223, no. 10–11 (2009): 1395–1406.

4. E. Peled, D. Golodnttsky, G. Ardel, C. Menachem, D. Bar Tow, and V. Eshkenazy, "The Role of SEI in Lithium and Lithium Ion Batteries," *MRS Online Proceedings Library (OPL)* 393 (1995): 209.

5. M. Gauthier, T. J. Carney, A. Grimaud, et al., "Electrode–electrolyte Interface in Li-Ion Batteries: Current Understanding and New Insights," *Journal of Physical Chemistry Letters* 6, no. 22 (2015): 4653–4672.

6. J. Lu, T. Wu, and K. Amine, "State-of-the-Art Characterization Techniques for Advanced Lithium-Ion Batteries," *Nature Energy* 2, no. 3 (2017): 1–13.

7. W. Wheeler, Y. Bultel, P. Venet, A. Sari, and E. Riviere, "Postmortem Analysis of 18650 Graphite/LFP Cells in a Long-Term Aging Study for Second-Life Applications," *Batteries* 10, no. 4 (2024): 119.

8. R. Azmi, F. Lindgren, K. Stokes-Rodriguez, et al., "An XPS Study of Electrolytes for Li-Ion Batteries in Full Cell LNMO vs Si/Graphite," *ACS Applied Materials & Interfaces* 16, no. 26 (2024): 34266–34280.

9. A. Skurtveit, E. T. North, H. Park, D. Chernyshov, D. S. Wragg, and A. Y. Koposov, "Stepwise Structural Relaxation in Battery Active Materials," *ACS Materials Letters* 7, no. 1 (2025): 343–349.

10. F. Shi, P. N. Ross, H. Zhao, G. Liu, G. A. Somorjai, and K. Komvopoulos, "A Catalytic Path for Electrolyte Reduction in Lithium-Ion Cells Revealed by In Situ Attenuated Total Reflection-Fourier Transform Infrared Spectroscopy," *Journal of the American Chemical Society* 137, no. 9 (2015): 3181–3184.

11. T. Kim, M. Cho, and K. Kwak, "Quantitative Analysis of the Li-Ion Solvation Structure in Li-Ion Battery Electrolytes Using ATR-FTIR Spectroscopy," *Analytical Chemistry* 96, no. 40 (2024): 15924–15930.

12. N. Saqib, C. M. Ganim, A. E. Shelton, and J. M. Porter, "On the Decomposition of Carbonate-Based Lithium-Ion Battery Electrolytes Studied Using Operando Infrared Spectroscopy," *Journal of the Electrochemical Society* 165, no. 16 (2018): A4051.

13. D. A. D. Corte, G. Caillon, C. Jordy, J.-N. Chazalviel, M. Rosso, and F. Ozanam, "Spectroscopic Insight into Li-Ion Batteries during Operation: An Alternative Infrared Approach," *Advanced Energy Materials* 6 (2016): 1501768.

14. C. Marino, A. Boulaoued, J. Fullenwarth, et al., "Solvation and Dynamics of Lithium Ions in Carbonate-Based Electrolytes during Cycling Followed by Operando Infrared Spectroscopy: The Example of $NiSb_2$, a Typical Negative Conversion-Type Electrode Material for Lithium Batteries," *Journal of Physical Chemistry Letters* 121, no. 48 (2017): 26598–26606.

15. M. Ayache, S. F. Lux, and R. Kostecki, "IR Near-Field Study of the Solid Electrolyte Interphase on a Tin Electrode," *The Journal of Physical Chemistry Letters* 6, no. 7 (2015): 1126–1129.

16. V. K. Peterson, M. Bianchini, K. W. Chapman, et al., "Terms of Latin Origin Relating to Sample Characterization (IUPAC Technical Report)," *Pure and Applied Chemistry* 96 (2024): 1531–1540.

17. D. A. Della Corte, *"Effects of Surface Chemical Treatment on Silicon Negative Electrodes for Lithium-Ion Batteries: an In Situ Infrared Spectroscopic Study*," PhD Thesis; Ecole Polytechnique, Palaiseau (France) (2013).

18. H. R. Phillip and E. A. Taft, "Kramers-Kronig Analysis of Reflectance Data for Diamond," *The Physical Review* 136, no. 5A (1964): A1445.

19. M. Moosavi, A. Motahari, A. Vahid, V. Akbar, A. A. Rostami, and A. Omrani, "Densities, Viscosities, and Refractive Indices of Dimethyl Carbonate +1-Hexanol/1-Octanol Binary Mixtures at Different Temperatures," *Journal of Chemical and Engineering Data* 61, no. 6 (2016): 1981–1991.

20. K. Hagiyama, K. Suzuki, M. Ohtake, et al., "Physical Properties of Substituted 1,3-Dioxolan-2-Ones," *Chemistry Letters* 37, no. 2 (2008): 210–211.

21. Z. Wang, G. Ren, H. Zhang, et al., "Measurement and Correlation of the Binary Systems Containing Vinylene Carbonate, Fluoroethylene Carbonate, and Chloroethylene Carbonate at 0.4 kPa," *Journal of Chemical and Engineering Data* 70, no. 2 (2025): 993–1003.

22. A. Nedjalkov, J. Meyer, A. Gräfenstein, et al., "Refractive Index Measurement of Lithium Ion Battery Electrolyte with Etched Surface Cladding Waveguide Bragg Gratings and Cell Electrode State Monitoring by Optical Strain Sensors," *Batteries* 5, no. 1 (2019): 30.

23. W. Wahyudi, V. Ladelta, L. Tsetseris, et al., "Lithium-Ion Desolvation Induced by Nitrate Additives Reveals New Insights into High Performance Lithium Batteries," *Advanced Functional Materials* 31, no. 23 (2021): 2101593.

24. B. Ludwig, Z. Zheng, W. Shou, Y. Wang, and H. Pan, "Solvent-Free Manufacturing of Electrodes for Lithium-Ion Batteries," *Scientific Reports* 6, no. 1 (2016): 23150.

25. M. T. Sougrati, S. Jouen, and B. Hannoyer, "Relative Lamb–Mössbauer Factors of Tin Corrosion Products," *Hyperfine Interactions* 167, no. 1–3 (2006): 815–818.

26. M. Masia, M. Probst, and R. Rey, "Ethylene Carbonate-$Li^+$: A Theoretical Study of Structural and Vibrational Properties in Gas and Liquid Phases," *The Journal of Physical Chemistry B* 108, no. 6 (2004): 2016–2027.

27. F. Shi, H. Zhao, G. Liu, P. N. Ross, G. A. Somorjai, and K. Komvopoulos, "Identification of Diethyl 2,5-Dioxahexane Dicarboxylate and Polyethylene Carbonate as Decomposition Products of Ethylene Carbonate Based Electrolytes by Fourier Transform Infrared Spectroscopy," *Journal of Physical Chemistry C* 118, no. 27 (2014): 14732–14738.

28. C. L. Angell, "The Infra-Red Spectra and Structure of Ethylene Carbonate," *Transactions of the Faraday Society* 52 (1956): 1178–1183.

29. P. Lanz and P. Novák, "Combined In Situ Raman and IR Microscopy at the Interface of a Single Graphite Particle with Ethylene Carbonate/Dimethyl Carbonate," *Journal of the Electrochemical Society* 161, no. 10 (2014): A1555.

30. J. Li, W. Yao, Y. S. Meng, and Y. Yang, "Effects of Vinyl Ethylene Carbonate Additive on Elevated-Temperature Performance of Cathode Material in Lithium Ion Batteries," *Journal of Physical Chemistry C* 112, no. 32 (2008): 12550–12556.

31. N. R. Bishnu Prasad Kar, K. Sundararajan, and K. S. Viswanathan, "Matrix Isolation and DFT Study of the Conformations of Diethylcarbonate," *Journal of Molecular Structure* 1072 ( 2014): 61–68.

32. C. Gervillié-Mouravieff, C. Boussard-Plédel, C. L. Jiaqiang Huang, et al., "Unlocking Cell Chemistry Evolution with Operando Fibre Optic Infrared Spectroscopy in Commercial Na(Li)-Ion Batteries," *Nature Energy* 7, no. 12 (2022): 1157–1169.

33. I. Noda, "Generalized Two-Dimensional Correlation Method Applicable to Infrared, Raman, and Other Types of Spectroscopy," *Applied Spectroscopy* 47 ( 1993): 1329–1336.

34. I. Noda, Chapter-2-Advances in Two-Dimensional Correlation Spectroscopy (2DCOS), in Frontiers and Advances in Molecular Spectroscopy, edited by J. Laane; (Elsevier Science, 2018) ISBN 97-8-0-1-2-81122-0-5.

35. Y.-Q. Wang, H. Xu, B. Cao, J. Ma, and Z.-W. Yu, "In Situ Species Analysis of a Lithium-Ion Battery Electrolyte Containing LiTFSI and Propylene Carbonate," *The Journal of Physical Chemistry Letters* 15, no. 19 (2024): 5047–5055.

36. J. Chouvin, J. Olivier-fourcade, J.-C. Jumas, et al., "SnO Reduction in Lithium Cells: Study by X-Ray Absorption, $^{119}$Sn Mössbauer Spectroscopy and X-Ray Diffraction," *Journal of Electroanalytical Chemistry* 494 (2000): 136–146.

37. P. Verma, P. Maire, and P. Novák, "A Review of the Features and Analyses of the Solid Electrolyte Interphase in Li-Ion Batteries," *Electrochimica Acta* 55, no. 22 (2010): 6332–6341.

## Supporting Information

Additional supporting information can be found online in the Supporting Information section. **Supporting Fig. S1:** Capacity profile comparison between a coin cell and the proposed in situ cell for the nano-tin electrode. **Supporting Fig. S2:** Current profile for *operando* infrared monitoring of nano-tin electrode at constant po tential experiment.